Volume 15, Issue 3, 152528 (1-16)

Iranian Journal of Catalysis (IJC)

https://doi.org/10.57647/j.ijc.2025.1503.28

Thermal decomposition synthesis of novel quaternary heterojunction $CuS/Cu_9S_5/Cu_2O/C_3N_4$ composites for enhanced visible-light-driven photocatalytic activity

Prakasit Intaphong[1,2,*], Pasu Inphak[1,2], Sujitra Tandorn[3], Pongpen Kaewdee[3], Komsanti Chokethawai[4], Chamnan Randorn[1,5]

[1]*Department of Chemistry, Faculty of Science, Chiang Mai University, Chiang Mai, 50200, Thailand.*
[2]*Multidisciplinary and Interdisciplinary School, Chiang Mai University, Chiang Mai, 50200, Thailand.*
[3]*Office of Research Administration, Chiang Mai University, Chiang Mai, 50200, Thailand.*
[4]*Department of Physics and Materials Science, Faculty of Science, Chiang Mai University, Chiang Mai, 50200, Thailand.*
[5]*Centre of Excellence in Materials Science and Technology, Chiang Mai University, Chiang Mai, 50200, Thailand.*

[*]**Corresponding author:** intaphong.p@gmail.com

Original Research

Received:
25 January 2025
Revised:
29 April 2025
Accepted:
29 May 2025
Published online:
1 July 2025
Published in issue:
30 September 2025

Abstract:

The novel quaternary heterojunction copper sulfide/cuprous sulfide/cuprous oxide/carbon nitride ($CuS/Cu_9S_5/Cu_2O/C_3N_4$) composite was prepared by thermal decomposition. The phase, composition, morphologies, and oxidation state of elements in as-prepared heterojunction multiphase Cu-based composites were characterized and discussed in this research. The XRD, SEM, and TEM analyses showed the binary CuS/Cu_9S_5 composite at 400 – 450 °C and quaternary heterojunction $CuS/Cu_9S_5/Cu_2O/C_3N_4$ composite at 500 – 600 °C, which presented the mixed irregular sheets and agglomerated particles in shape. The photocatalytic activities of heterojunction multiphase Cu-based composites were studied by methyl orange (MO) degradation under visible light irradiation. It was found that the $CuS/Cu_9S_5/Cu_2O/C_3N_4$ composite at 600 °C showed the highest photodegradation efficiencies of MO at 90.06% under visible light irradiation within 150 min due to the charge diffusion at the $CuS/Cu_9S_5/Cu_2O/C_3N_4$ interface. The active species for MO degradation over $CuS/Cu_9S_5/Cu_2O/C_3N_4$ composite were analyzed by scavenger test, which reveals that the $^{\bullet}O_2^-$ radicals and h^+ are the main and minor active species for MO degradation photocatalyzed by the $CuS/Cu_9S_5/Cu_2O/C_3N_4$ composite under visible light irradiation. Finally, the photodegradation efficiency of MO in the presence of the $CuS/Cu_9S_5/Cu_2O/C_3N_4$ composite at 600 °C decreased to 85.89% after five cycles, demonstrating its stability and reusability for practical photocatalytic applications.

Keywords: Cu-based composite; Cu-thiourea; Heterojunction; Photocatalytic activity; Thermal decomposition

1. Introduction

In recent years, wastewater effluents from textile industries, agricultural activities, and human activities have been released into the environment, posing significant risks to multiple detrimental effects on natural ecosystems due to their carcinogenic, mutagenic, and toxic effects on living organisms [1–3]. Methyl orange ($C_{14}H_{14}N_3NaO_3S$; MO), an organic xanthene dye, is highly water-soluble and characterized by its distinctive orange-red color. It is widely used in the textile, printing, paper, pharmaceutical, and food industries, which are frequently released into the environment without proper treatment [4–8]. It is an allergic reaction to the mutagenic, carcinogenic, allergenic substances, neurotoxicity, and chronic toxic effects on humans and animals [5, 6]. Conventional wastewater treatment methods, including biochemical, chemical, and physical treatment methods, are limited due to the formation of secondary toxic byproducts and the incomplete removal of pollutants [9, 10]. Photocatalysis process, as a green technology, is highly efficient for wastewater treatment, as semiconductor photocatalysts create highly reactive oxygen species under light irradiation, degrading toxic organic pollutants into harmless byproducts such as CO_2, H_2O, and inorganic anions [11–15]. Photocat-

alytic technology is a cost-effective water treatment method that is highly stable, has no secondary pollution, and offers potential utilization of solar energy and mineralization [16–18].

Various traditional photocatalysts, including TiO_2, ZnO, and CuO, exhibit high photocatalytic performance, cost-effectiveness, non-toxicity, and environmental friendliness [19–22]. Titanium dioxide (TiO_2), with a band gap of 3.2 eV, is the most widely used photocatalyst but is active in only the UV region, which constitutes approximately 5% of solar energy [17, 18, 23, 24]. Therefore, current research is focused on visible-light-driven semiconductors as photocatalysts for pollutant degradation, as the visible light region accounts for approximately 43% of the solar spectrum [16–18, 25, 26].

Semiconductor copper (II) compounds-based photocatalyst, copper oxide (CuO) with a narrow band gap of 1.7 eV has garnered significant interest for applications in photocatalysis [27, 28], gas sensors [29], lithium batteries [30], and solar cells [31] due to their outstanding optical, magnetic, and electric properties. Copper sulfides (CuxS), where $x = 0.5 - 2$, are among the most important representatives of metal chalcogenides, which have been extensively studied in recent decades [32–34]. CuS, a metal sulfide semiconductor with a narrow band gap of $2.0 - 2.2$ eV, shows the unique optical and electrical properties [35, 36]. CuxS with $x = 1.8 - 2.0$ is a suitable and efficient semiconductor material for solar cells and optoelectronic devices [32, 37, 38]. However, the photocatalytic performance of single semiconductor copper (II) compounds-based photocatalysts is relatively low for dye degradation due to rapid photoinduced carrier recombination, poor light absorption, weak redox capacity, and low stability [16, 27, 28]. To address these challenges, heterojunction multiphase Cu-based composites have gained significant attention, as they facilitate the separation of photogenerated charge carriers, enhance visible light absorption and provide higher active surface area, leading to the generation of more reactive species compared to single-component copper (II) compounds-based photocatalyst, thereby improving photocatalytic performance [39–46]. For example, L. Han et al. fabricated the Cu_2O/CuO core-shell nanowires directly on a Cu mesh for methylene blue (MB) degradation under visible light irradiation [44]. C. Wang et al. reported excellent MO and MB degradation under UV light irradiation in present of CuS/CuO nanorod arrays on Cu mesh [45]. According to S. Mosleh et al., as-prepared $CuO/Cu_2O/Cu$ nanoparticles demonstrated excellent photocatalytic degradation of safranin O (SO) and MB under blue light-emitting diode (LED) irradiation [46]. In addition, graphitic carbon nitride (g-C_3N_4), a metal-free polymeric photocatalyst, has attracted considerable interest for environmental purification when combined with other semiconductor photocatalysts due to its unique physicochemical properties, simple synthesis, thermal stability, high charge transport efficiency, and strong light-harvesting ability [47–53]. The integration of g-C_3N_4 with other semiconductor photocatalysts such as $ZnO/CuO/g\text{-}C_3N_4$ [54], $g\text{-}C_3N_4/CuS$ [55], $g\text{-}C_3N_4/Cu_2O$ [56], $ZnO/g\text{-}C_3N_4$ [57] and $Ag_3PO_4/Co_3(PO_4)_2/g\text{-}C_3N_4$ [58] increase the facilitate charge carrier transfer and enhances photocatalytic activity compared to pure g-C_3N_4. For example, M. Cai et al. synthesized the S-scheme photosystem of oxygen vacancy (OV)-rich Bi_2WO_6/C_3N_4/carbon fiber cloth for the photocatalytic degradation of tetracycline (TC) and Cr(VI) photoreduction under visible light irradiation [51]. The Bi_2WO_6/C_3N_4/carbon fiber cloth showed excellent reusability and easy recovery for industrial applications. Similarly, W. Shi et al. reported that ternary $Ag_3PO_4/Co_3(PO_4)_2/g\text{-}C_3N_4$ composites demonstrated superior photocatalytic performance for TC degradation under visible light irradiation compared to single semiconductor $Co_3(PO_4)_2$, g-C_3N_4, and the binary $Co_3(PO_4)_2/g\text{-}C_3N_4$ composite. This enhancement was attributed to the formation of a Z-scheme and Type II heterojunction among Ag_3PO_4, $Co_3(PO_4)_2$, and g-C_3N_4, which promoted effective charge separation [58].

In this work, we report the synthesis of copper-based composites (CuS/Cu_9S_5 and $CuS/Cu_9S_5/Cu_2O/C_3N_4$) by a one-step thermal decomposition method using Cu-thiourea as a precursor. The objective is to obtain quaternary heterojunction $CuS/Cu_9S_5/Cu_2O/C_3N_4$ composites to enhance visible-light-driven photocatalysis. The phase, composition, morphology, oxidation state, and optical properties of the synthesized $CuS/Cu_9S_5/Cu_2O/C_3N_4$ composite were analyzed using X-ray diffraction (XRD), scanning electron microscopy (SEM), transmission electron microscopy (TEM), UV-Vis diffuse reflectance spectroscopy (DRS), X-ray photoelectron spectroscopy (XPS), Brunauer-Emmett-Teller (BET) surface area analysis, and photoluminescence spectroscopy (PL) and discussed in this research. The photocatalytic activity of the $CuS/Cu_9S_5/Cu_2O/C_3N_4$ composite was studied by degradation of MO, an anionic synthetic xanthene dye, under visible light irradiation. Furthermore, the photocatalytic mechanism and photocatalytic stability of the $CuS/Cu_9S_5/Cu_2O/C_3N_4$ composite were investigated and proposed based on experimental results.

2. Experimental method

2.1 Preparation and characterization of copper-based composites by thermal decomposition method

The Cu-thiourea (pentakis(thiourea)dicopper(I)sulfate) compound was prepared by dissolving 2.5 g of thiourea (NH_2CSNH_2) in 15 mL of distilled water and 2.5 g of copper (II) sulfate pentahydrate ($CuSO_4{\cdot}5H_2O$) in another 15 mL of distilled water at room temperature. The $CuSO_4{\cdot}5H_2O$ and NH_2CSNH_2 solutions were then cooled in an ice bath under continuous stirring. Subsequently, the $CuSO_4{\cdot}5H_2O$ solution was slowly added into the NH_2CSNH_2 solution in an ice bath to obtain the white crystals. Next, 1.0 g of NH_2CSNH_2 was weighed, dissolved in 10 mL of distilled water, and added to the mixture under vigorous stirring. Finally, the as-prepared white Cu-thiourea crystals, used as the starting material, were filtered using a Hirsch or Büchner funnel, washed, and dried at 80 °C for 12 h in the oven.

To prepare copper-based composites by the thermal decomposition method, 2.5 g of the as-prepared Cu-thiourea (pentakis(thiourea)dicopper(I)sulfate) sample was weighed

and placed in an alumina ceramic crucible boat, which was transferred to an electric tube furnace. The sample was heated at 400, 450, 500, 550, and 600 °C for two hours with a heating rate of 10 °C. min^{-1} and a nitrogen (N_2) gas flow of 100 mL/min to prevent oxidation of the copper compound. After cooling, the as-synthesized copper-based composite was collected and ground for further characterization. A schematic illustration of the synthesis procedure for $CuS/Cu_9S_5/Cu_2O/C_3N_4$ composites by the thermal decomposition method is shown in Fig. 1.

The phase and composition of copper-based composites were analyzed by Rigaku™ Miniflex 600 X-ray diffractometer (XRD) equipped with a monochromatic Cu K_α as X-ray source (λ = 1.54056 Å). The XRD patterns were recorded over a 2θ range of $10^\circ - 60^\circ$ with a scanning rate of 0.01° sec^{-1}. The obtained XRD data were analyzed by X'Pert HighScore Plus software and compared with reference patterns from the Joint Committee on Powder Diffraction Standards (JCPDS). The morphologies of the copper-based composites were investigated by TESCAN VEGA III scanning electron microscope (SEM) operating at 15 kV with Au sputter coating and JEM-2010 JEOL transmission electron microscopy (TEM) operating at 200 kV. All composite samples were sonicated in absolute ethanol and dropped onto copper tape for SEM analysis and onto a 200-mesh carbon-coated copper grid for TEM analysis. The optical absorption properties of the samples were measured using a PerkinElmer-Lambda 365 Plus UV-visible diffuse reflectance spectrophotometer (DRS) at $200 - 800$ nm. The oxidation state and elemental composition of the copper-based composites were analyzed using an Axis Ultra DLD Kratos Analytical Ltd X-ray photoelectron spectrometer (XPS) equipped with a monochromatic Al K_α as an excitation source (λ = 1486.6 eV). The binding energy was calibrated using the C 1 s peak at 285.1 eV as a reference. The photoluminescence (PL) spectra of the samples were measured on the Horiba model FluoroMax Plus spectrofluorometer. The specific surface area and pore volume of the composite were determined using nitrogen adsorption–desorption isotherm on a Quantachrome Autosorb-1 MP analyzer at 77 K.

2.2 Photocatalytic performance of copper-based composites

The methyl orange (MO), as an anionic synthetic xanthene dye, was monitored for photocatalytic activity over copper-based composites under visible light irradiation. A 0.0045 g of copper-based composite was dispersed in 30.0 mL of a 1.0×10^{-5} M MO solution and stirred in the dark conditions for 30 min at 25 °C with a cooled water circulating to establish adsorption-desorption equilibrium between the dye and the photocatalyst. Following equilibration, the suspension was irradiated with visible light from a 50 W visible LED lamp with an irradiation power of 0.565 mW/cm^2, positioned 2.5 cm from the reaction system. At 30 min intervals, 2.0 mL of the MO suspension was sampled, centrifuged to remove the photocatalyst precipitate, and analyzed for MO concentration at maximum absorption wavelength (λ_{max}) of 464 nm using Spectroquant® Prove 300 UV-Vis spectrosphotometer. The degradation efficiency was calculated by the following equation:

$$\text{Degradation efficiency}(\%) = (C_0 - C_t)/C_t \times 100 \quad (1)$$

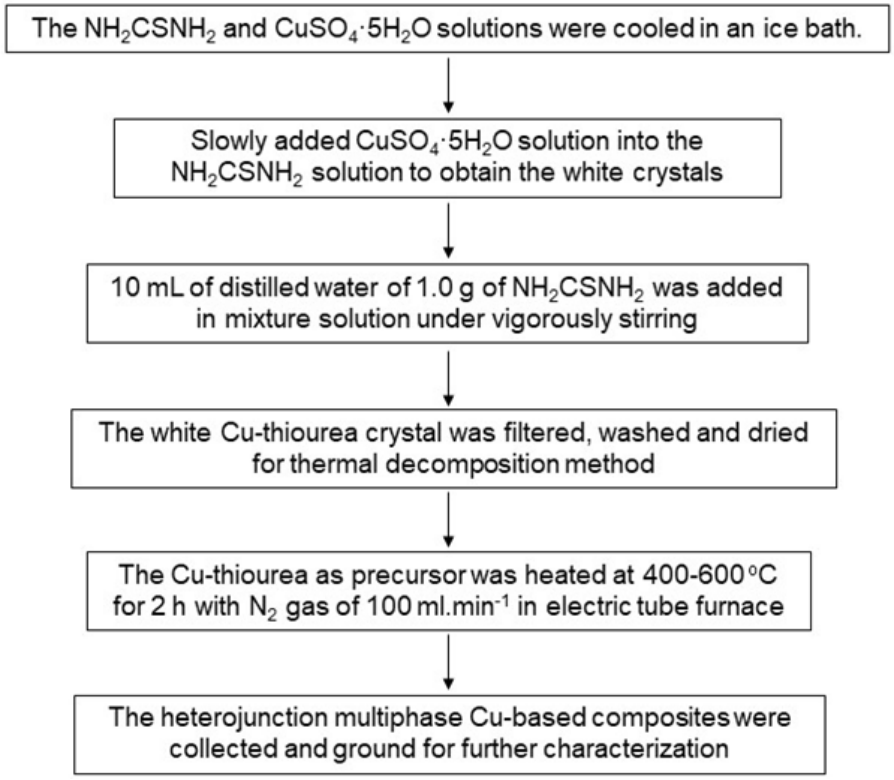

Figure 1. A scheme synthesis procedure of the $CuS/Cu_9S_5/Cu_2O/C_3N_4$ composites by thermal decomposition method.

where C_0 is the initial dye concentration and C_t is the dye concentration after photocatalytic treatment for a given time (t). The photocatalytic stability of the composites was tested for five cycles under the same conditions under visible light irradiation. At the end of each photocatalytic cycle, the used photocatalyst was recovered by centrifugation, washed, and dried at 80 °C for 12 h before reuse in the next MO degradation experiment. Finally, the product species after photocatalytic reaction over $CuS/Cu_9S_5/Cu_2O/C_3N_4$ at 600 °C were analyzed by a 2690 LCT Micromass electrospray ionization (ESI) mass spectrometer in negative ion mode.

3. Results and discussion

3.1 Characterization of copper-based composites

The phase composition and structure of heterojunction multiphase Cu-based composites synthesized by thermal decomposition of Cu-thiourea complexes at 400 – 600 °C for two h under an N_2 atmosphere were analyzed by XRD as shown in Fig. 2. XRD pattern of Cu-thiourea complex thermally decomposed at 400 °C for two h revealed eight distinct diffraction peaks at $2\theta = 27.16°$, 27.71°, 29.31°, 31.82°, 32.87°, 47.99°, 52.77° and 58.74° which can be assigned to the Miller index of (100), (101), (102), (103), (006), (108), (114) and (203) crystallographic planes of a hexagonal CuS structure with according to the JCPSD No. 79-2321 as standard. However, it found the minor diffraction peak at $2\theta = 46.17$, which can be assigned to the Miller index of the (111) crystallographic plane of the rhombohedral Cu_9S_5 structure, according to the JCPSD No. 47-1748 as standard. The intensity of diffraction at (103) crystallographic planes of the hexagonal CuS structure is higher than that of the diffraction peak of (111) crystallographic planes of the rhombohedral Cu_9S_5 structure, indicating that the hexagonal CuS structure is the major phase and the rhombohedral Cu_9S_5 structure is the minor phase were synthesized at this stage [59, 60]. At 450 °C, the mixed-phase structure of hexagonal CuS and rhombohedral Cu_9S_5 persisted. However, it can see that the intensity of (103) planes of hexagonal CuS structure was decreased whereas the intensity of (111) crystallographic planes of rhombohedral Cu_9S_5 structure was increased, indicating that the rhombohedral Cu_9S_5 structure and hexagonal CuS structure were major and minor phases at this 450 °C due to the hexagonal CuS structure was transferred to completely rhombohedral Cu_9S_5 structure [59, 60]. Upon increasing the thermal decomposition temperature to 500 – 600 °C, the formation of a new two-structure, hexagonal C_3N_4, and cubic Cu_2O phases was detected. The appearance of new diffraction peak at $2\theta = 15.91°$ and 35.87° can be assigned to the Miller index of (100) and (101) crystallographic planes of hexagonal C_3N_4 structure (JCPSD No. 50-1250) which are corresponding to the typical interplanar structural packing and interlayer stacking structure of C_3N_4, respectively [61], according to Y. Hong et al. reported the ultratthat hin g-C_3N_4 nanosheets were synthesized by calcination of thiourea at 500 °C [62]. Moreover, new diffraction peaks at $2\theta = 36.42°$, 42.30°, and 61.34° can be assigned to the Miller index of (111), (200), and (220) crystallographic planes of cubic Cu_2O phases (JCPSD No. 05-0667). According to the previous study by C. M. Simonescu et al., thermal decomposition of CuS can result in the formation of nonstoichiometric CuxS, accompanied by oxidation of sulfur to SO_2, which subsequently reacts with Cu_2O and O_2 to form cuprous oxides (Cu_2O) and oxysulfates [63]. Therefore, the quaternary heterojunction $CuS/Cu_9S_5/Cu_2O/C_3N_4$ composites were successful synthesized by thermal decomposition of Cu-thiourea complexes at 500 – 600 °C for two h under an N_2 atmosphere. The phase and composition of heterojunction multiphase Cu-based composites were summarized in Table 1.

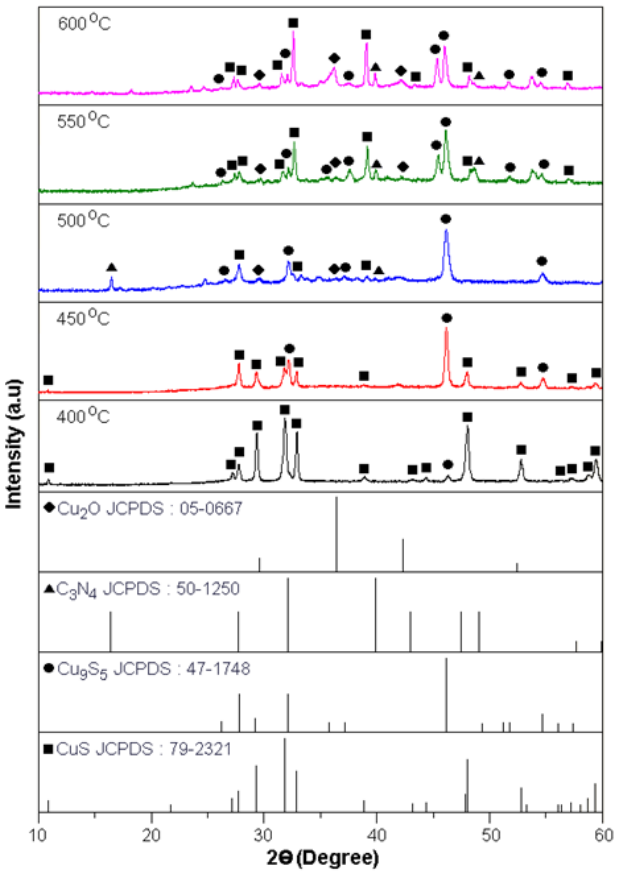

Figure 2. XRD patterns of as-prepared samples synthesized by thermal decomposition method at 400 – 600 °C for 2 h.

The morphology of the synthesized heterojunction multiphase Cu-based composites was investigated using SEM, as shown in Fig. 3. It was observed that the morphologies of CuS/Cu_2S phase at 400 and 450 °C (Fig. 3 (a) and 3 (b)) revealed a mixed agglomerate dispersion of microparticles islands with particle size of $2 - 3$ μm supported on the highly ordered nanoplates with particle size of $200 - 500$ nm. The aggolerated microparticles islands are composed of nanoparticles with an approximate size of 100 nm. When the synthesis temperature was increased to 500 and 550 °C, the $CuS/Cu_9S_5/Cu_2O/C_3N_4$ composite exhibited well-dispersed nanoparticles with a size of $80 - 100$ nm supported on the smaller agglomerated nanoplates and nanosheets with a size of $0.8 - 1.0$ μm. This mixed morphology of nanoplates and nanosheets formed a porous hierarchical structure. However, the mor-

Table 1. Composition and phase percentages of samples synthesized by thermal decomposition method.

Thermal decomposition temperature (°C)	Percentage of phase (%)			
	CuS	**Cu_9S_5**	**Cu_2O**	**C_3N_4**
400 °C	81.63 %	18.37 %	-	-
450 °C	31.40 %	68.60 %	-	-
500 °C	47.01 %	19.85 %	13.12 %	20.02 %
550 °C	36.67 %	31.13 %	15.46 %	16.74 %
600 °C	27.51 %	37.41 %	20.27 %	15.93 %

phologies of $CuS/Cu_9S_5/Cu_2O/C_3N_4$ sample at 600 °C (Fig. 3 (e)) show the formation of excellent dispersion of porous nanoparticles with size of $100-200$ nm on the surface of layered microplates with the size range of $0.5-2.0$ μm to create the heterojunction quaternary $CuS/Cu_9S_5/Cu_2O/C_3N_4$ composites.

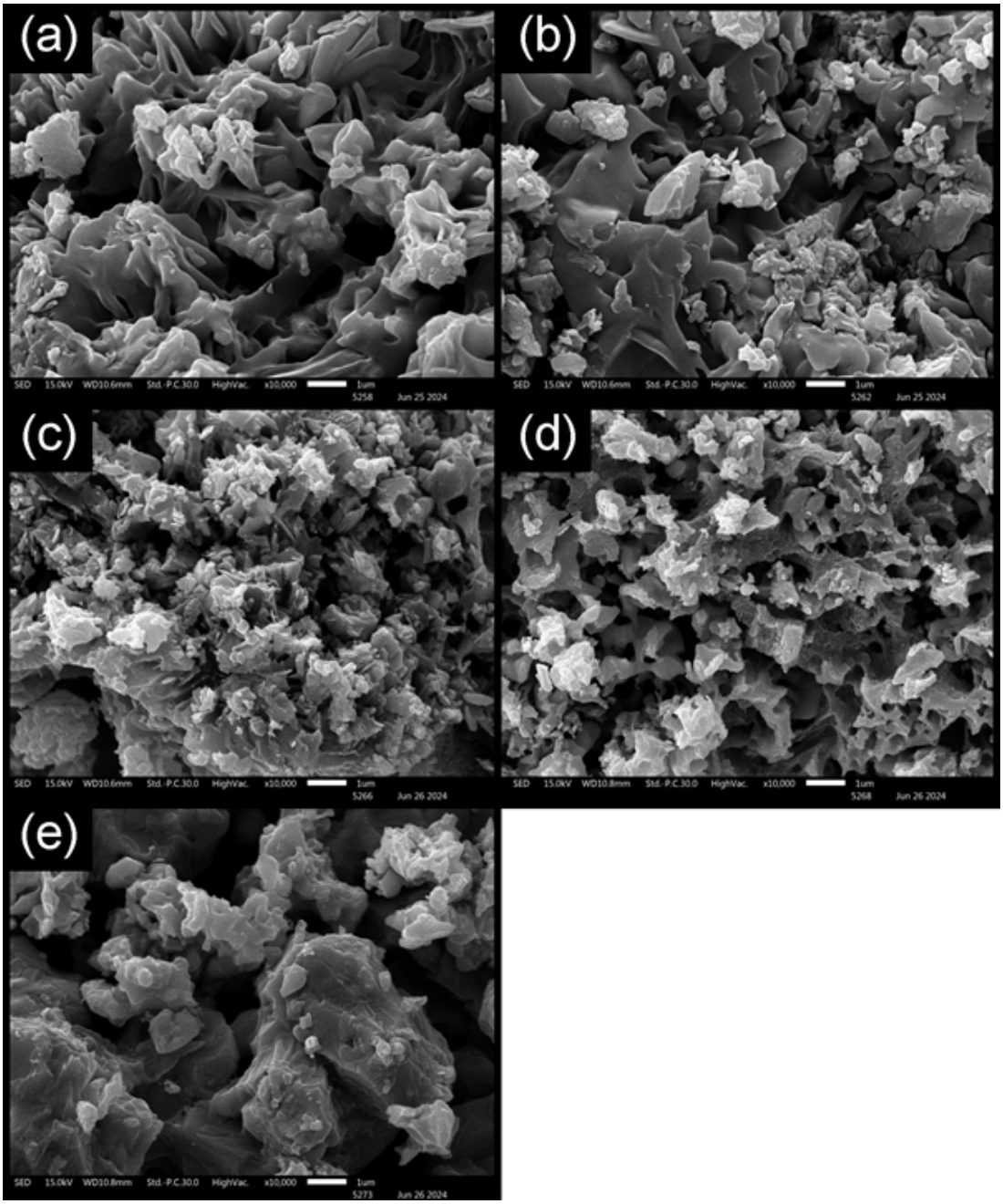

Figure 3. SEM images of as-prepared samples synthesized by thermal decomposition method at (a) 400, (b) 450, (c) 500, (d) 550 and (e) 600 °C for 2 h.

To further investigate the structure interactions of the samples prepared by thermal decomposition were observed by TEM. The morphologies of binary CuS/Cu_9S_5 composite at 400 °C (Fig. 4 (a)) consist of numerous thin sheet. Fig. 4 (b) shows a TEM image of the CuS/Cu_9S_5 sample at 500 °C, revealing stacked nanosheets with an average size of 80 – 200 nm with spherical nanoparticles attached to their surfaces. Figs. 4 (c-e) illustrate the TEM images of quaternary $CuS/Cu_9S_5/Cu_2O/C_3N_4$ composites synthesized at 500 – 600 °C. They reveal that the morphologies of quaternary heterojunction $CuS/Cu_9S_5/Cu_2O/C_3N_4$ samples consist of agglomerated nanoparticles supported on the thin nanosheets to form the heterojunction $CuS/Cu_9S_5/Cu_2O/C_3N_4$ composites. By TEM observation, the $Cu_3N/Cu_2O/C_3N_4/Cu$ samples at 500 – 600 °C display lower agglomerate and size of nanoparticles and nanosheets than CuS/Cu_9S_5 samples at 400 – 450 °C, leading the higher active surface area and enhanced the photocatalytic reaction.

Fig. 5 presents the N_2 adsorption-desorption isotherms and the pore size distribution curves of heterojunction multi-

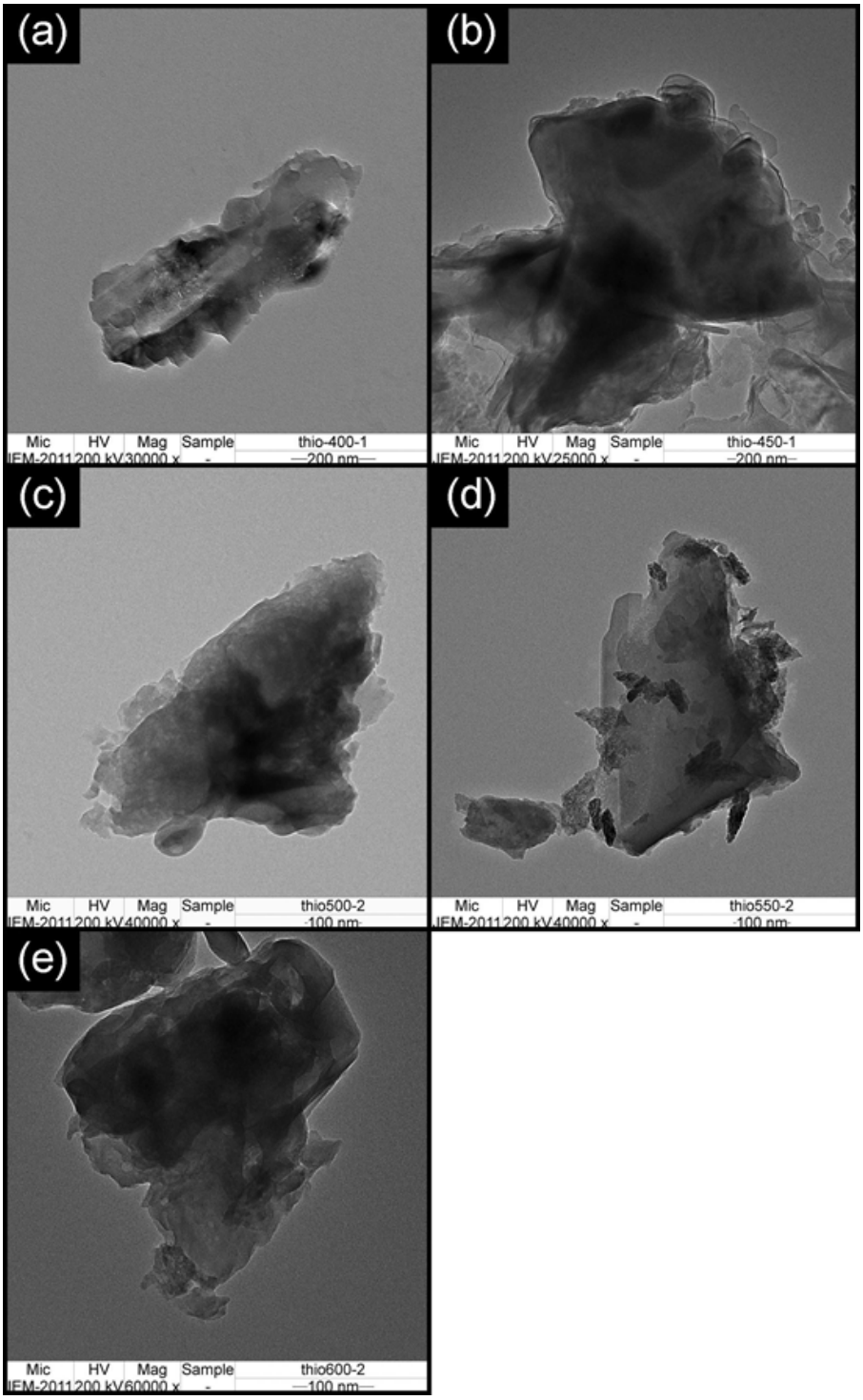

Figure 4. TEM images of as-prepared samples synthesized by thermal decomposition method at (a) 400, (b) 450, (c) 500, (d) 550 and (e) 600 °C for 2 h.

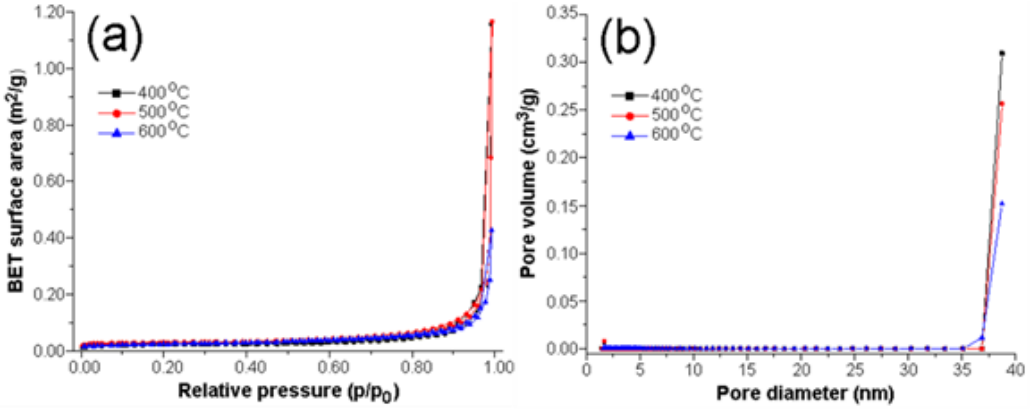

Figure 5. (a) BET surface area and (b) pore size of as-prepared samples synthesized by thermal decomposition method at 400, 500 and 600 °C for 2 h.

phase Cu-based composites synthesized at 400, 500, and 600 °C. The N_2 adsorption–desorption isotherms of all samples show the hysteresis loop of P/P_0 at $0.6-1.0$, which is according to the type IV with H_3 hysteresis loop by IUPAC classification, suggesting the heterojunction multiphase Cu-based composites at 400, 500, and 600 °C are mesoporous material [64–66]. The active surface areas of the sample were calculated using the Brunauer-Emmett-Teller (BET) method, which were 1.95, 2.55, and 1.79 m^2/g at 400, 500, and 600 °C, respectively. It was observed that the surface area of heterojunction multiphase Cu-based composites did not show a significant difference at $400-600$ °C, which indicates that the photocatalytic performance of heterojunction multiphase Cu-based composites does not depend on the active surface area of the sample in this research. The pore size of samples was calculated on the Barrett-Joyner-Halenda model, which showed a total pore volume and pore diameter of samples were 0.0402, 0.0404, and 0.0148 cm^3/g and 82.28, 63.42, and 33.02 nm for multiphase Cu-based composites at 400, 500, and 600 °C, respectively [64–66].

The elemental composition and chemical states of the $CuS/Cu_9S_5/Cu_2O/C_3N_4$ composite synthesized at 600 °C were examined using XPS as shown in Fig. 6 The full survey XPS spectrum at $0-1200$ eV of $CuS/Cu_9S_5/Cu_2O/C_3N_4$ composite (Fig. 6 (a)) show the binding energies of only Cu, S, C, N and O core levels, indicating that the presence of Cu, S, C, N and O elements in sample. Fig. 6 (b) shows the high-resolution binding energies of Cu 2p core level, which were deconvoluted into couple binding energies of Cu $2p_{3/2}$ and Cu $2p_{1/2}$ core levels at 932.52/952.83, 936.22/956.15, and 934.74/954.27 eV, which correspond to the three Cu species in CuS, Cu_9S_5, and Cu_2O compounds in the composite. The two binding energy peaks located at 932.52 eV for Cu $2p_{3/2}$ and 952.83 eV for Cu $2p_{1/2}$ of Cu 2p core level were assigned to Cu^{2+} species of CuS phase [67–69]. The binding energies of Cu 2p core level of Cu^+ species in Cu_9S_5 were detected at 936.22 eV for Cu $2p_{3/2}$ and 956.15 eV for Cu $2p_{1/2}$, according to the previous reports [70, 71]. However, the high-resolution energies peaks at 934.74 eV of Cu $2p_{3/2}$ and 954.27 eV of Cu $2p_{1/2}$ are assigned to the Cu^+ ions

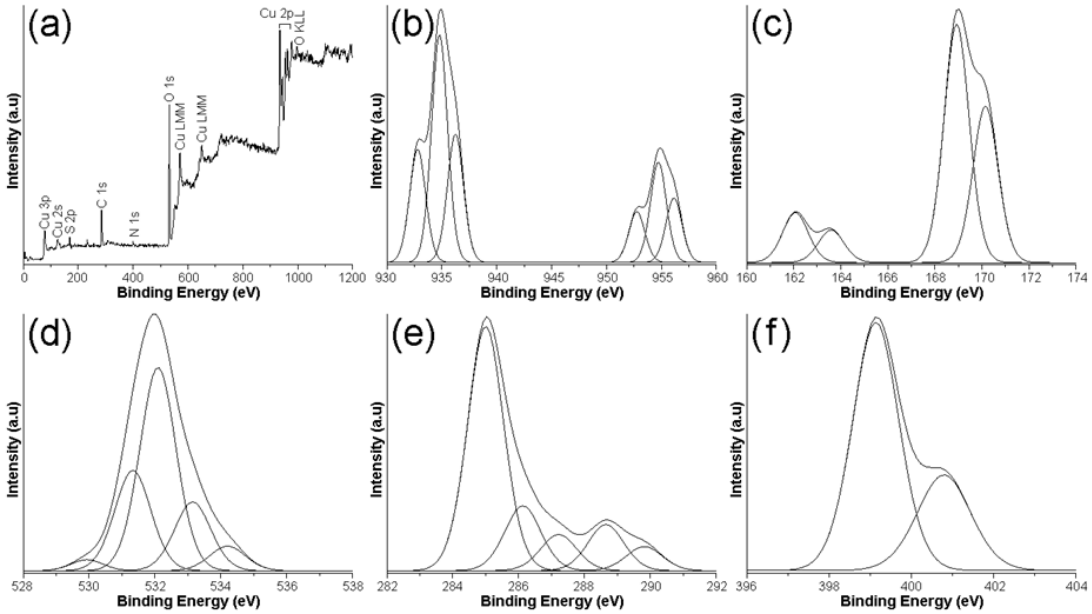

Figure 6. XPS spectra of (a) survey, (b) Cu 2p, (c) S 2p, (d) O 1s, (e) C 1s and (f) N 1s of $CuS/Cu_9S_5/Cu_2O/C_3N_4$ composite synthesized by thermal decomposition method at 600 °C for 2 h.

of Cu_2O in $CuS/Cu_9S_5/C_3N_4/Cu_2O$ composite [72, 73]. Fig. 6 (c) shows the binding energies peaks of S 2p core level which can be split into four binding energies peaks at 162.33/163.63 eV for S $2p_{3/2}$ spin orbits and 168.92/170.12 eV for S $2p_{1/2}$ spin orbit. The two symmetrical binding energies of the S $2p_{3/2}$ and S $2p_{1/2}$ spin orbits of S^{2-} ions in CuS were detected at 162.33 and 168.92 eV while the two symmetrical binding energies of the S $2p_{3/2}$ and S $2p_{1/2}$ spin orbits of S^{2-} ions in Cu_9S_5 were detected at 163.33 and 170.12 eV, confirming the formation of CuS and Cu_9S_5 in composite [69, 70, 74]. By Gaussian analysis, the binding energies peaks of O 1s core level (Fig. 6 (d)) were assigned to Cu-O bonding in Cu_2O phase (532.12 eV), the water absorption on sample surface (533.10 eV) and oxygen functional groups including the -COOH (529.92 eV), (531.32 eV) and C-O-C (534.22 eV) in g-C_3N_4 [75–78] while the binding energies peaks of C 1s core level (Fig. 6 (e)) are identified to the sp^2 C-C bonding (285.03 eV), C=N sp^2 (286.12 eV), C-N (287.25 eV), C-OH bonding (288.62 eV), and sp^2 N-C=N bonding (289.82 eV) in the triazine units of g-C_3N_4, respectively [77–79]. Finally, the tertiary nitrogen N-$(C)_3$ groups in the C_3N_4 phase were detected at 399.83 and 400.83 eV as shown in Fig. 6 (f) [79, 80].

Fig. 7 (a) shows the UV-vis DRS spectra of the as-prepared heterojunction multiphase Cu-based composites at 400 – 600 °C. The UV-vis DRS spectra of heterojunction multiphase Cu-based composites at 400 – 600 °C indicated excellent absorption in the UV-visible light region, with a significant enhancement in visible light absorption for the heterojunction $CuS/Cu_9S_5/Cu_2O/C_3N_4$ composites compared to the binary CuS/Cu_9S_5 phase. This enhancement is attributed to the formation of Cu_2O and C_3N_4, which improve photon utilization in the heterojunction system [56, 77]. The band gap (E_g) of the as-synthesized heterojunction multiphase Cu-based composites at 400 – 600 °C was determined using the Kubelka-Munk formula, as expressed in Eq. (2).

$$\alpha h\nu = A(h\nu - E_g)^{n/2} \quad (2)$$

where α is the absorption coefficient, h is Planck's constant, ν is the optical frequency, A is a proportionality constant, and n is the transition type of semiconductors [57, 73, 80]. Fig. 7 (b) shows the Tauc plot of $(\alpha h\nu)^2$ versus $h\nu$ of the heterojunction multiphase Cu-based composites at 400 – 600 °C. The calculated band gap energy of semiconductor photocatalysts decreased significantly from 2.03 eV at 400 °C to 1.62 eV at 600 °C. This reduction in band gap energy is attributed to the formation of C_3N_4 and Cu_2O in the binary CuS/Cu_9S_5 phase at high temperature. The band gap energy of quaternary heterojunction $CuS/Cu_9S_5/Cu_2O/C_3N_4$ composites was decreased compared to the binary CuS/Cu_9S_5 phase, which indicates a better light absorption capability, improving the visible-light-driven photocatalytic activity of heterojunction $CuS/Cu_9S_5/Cu_2O/C_3N_4$ composites [56, 67]. Moreover, the narrow band gap of the heterojunction $CuS/Cu_9S_5/Cu_2O/C_3N_4$ composites significantly enhances charge carrier generation and separation efficiency, further improving photocatalytic activity [81, 82].

3.2 The visible-light-driven photocatalytic activities of copper-based composites

The photocatalytic performances of the heterojunction multiphase Cu-based composites were evaluated based on the MO degradation under visible light irradiation. Fig. 8 shows the UV-visible absorption spectra of MO at different lengths of visible light irradiation time over the $CuS/Cu_9S_5/Cu_2O/C_3N_4$ composite synthesized at 600 °C for two h. It was observed that the λ_{max} of MO at 464 nm in the $CuS/Cu_9S_5/Cu_2O/C_3N_4$ composite at 600 °C for two h was decreased with increasing visible light irradiation time, indicating the degradation of MO molecules during the photocatalytic reaction [7, 8]. After 150 min, the absorption intensity of MO approached zero, indicating that the MO molecules were degraded by active species from heterojunction $CuS/Cu_9S_5/Cu_2O/C_3N_4$ composites under visible light irradiation. Furthermore, the initial dark yellow turned colorless after the photocatalytic reaction, further verifying the effective degradation of MO molecules by the active species in the $CuS/Cu_9S_5/Cu_2O/C_3N_4$ composite during visible-light-driven photocatalysis.

Fig. 9 (a) exhibits the photodegradation performance of MO over heterojunction multiphase Cu-based composites synthesized at 400 – 650 °C under visible light irradiation and MO solution without photocatalyst under visible light as a reference. The pure MO solution without

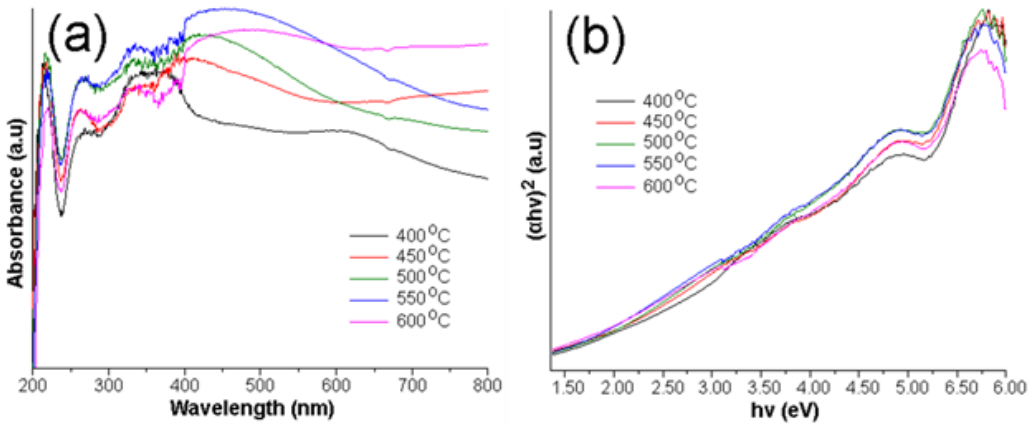

Figure 7. (a) DRS spectra and (b) band gaps of as-prepared samples synthesized by thermal decomposition method at 400 – 600 °C for 2 h.

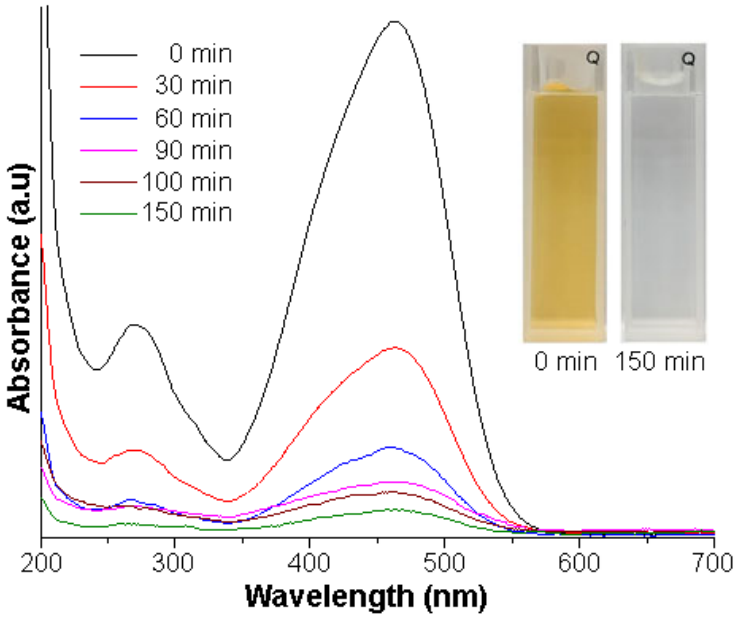

Figure 8. UV-Vis spectra of photodegradation of MO over $CuS/Cu_9S_5/Cu_2O/C_3N_4$ composite at 600 °C for 2h within different lengths of visible light irradiation time.

photocatalyst, when irradiated under visible light for 150 min, exhibited minimal photolysis, indicating that MO molecules are highly stable under visible light irradiation. The absorption of MO over the heterojunction multiphase Cu-based composites in the dark for 30 min was measured as 1.25%, 2.08%, 2.49%, 3.32%, 4.15%, and 4.09% for 400, 450, 500, 550, 600, and 650 °C, respectively. Notably, the $CuS/Cu_9S_5/Cu_2O/C_3N_4$ composite exhibited higher MO absorption in the dark compared to the CuS/Cu_9S_5 composite. This enhancement can be attributed to C_3N_4, which carries a positive surface charge, facilitating electrostatic interactions with anionic MO dye molecules, thereby increasing the photocatalytic reaction site on the $CuS/Cu_9S_5/Cu_2O/C_3N_4$ surface [75, 81]. Under visible light irradiation for 150 min, the MO degradation efficiencies of multiphase Cu-based composites were 30.02%, 44.56%, 79.12%, 84.77%, 90.06%, and 77.49% at 400, 450, 500, 550, 600, and 650 °C, respectively. The photocatalytic efficiency of multiphase Cu-based composites was increased from 30.02% at 400 °C to a maximum of 90.06% at 600 °C. However, the photocatalytic efficiencies of multiphase Cu-based composites at 650 °C were decreased to 77.49% under visible light irradiation within 150 min. The photocatalytic performances of the binary CuS/Cu_9S_5 composite were increased with the coupling phase of C_3N_4 and Cu_2O, which contributes to improved charge generation and reduced electron-hole recombination [83, 84]. The presence of C_3N_4 ($E_g = 2.7$ eV) and Cu_2O ($E_g = 2.17$ eV) facilitates efficient visible light absorption, thereby enhancing the photocatalytic performance [85]. According to the analytical results, the $CuS/Cu_9S_5/Cu_2O/C_3N_4$ at 600 °C shows superior visible light harvesting and efficient active species generation for MO degradation. Therefore, the phase composition and weight ratio of CuS, Cu_9S_5, Cu_2O, and C_3N_4 in the composition are key controls in photocatalytic performance. Fig. 10 shows the PL spectra of the multiphase Cu-based composites using an excitation wavelength of 225 nm. Generally, lower PL intensity in a photocatalyst

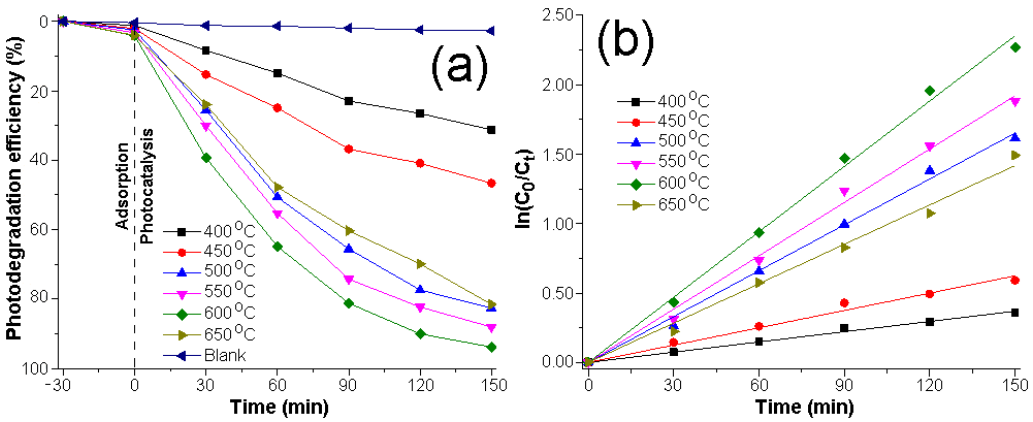

Figure 9. (a) Photodegradation efficiencies and (b) kinetic reaction of MO degradation by as-prepared samples synthesized by thermal decomposition method under visible light irradiation.

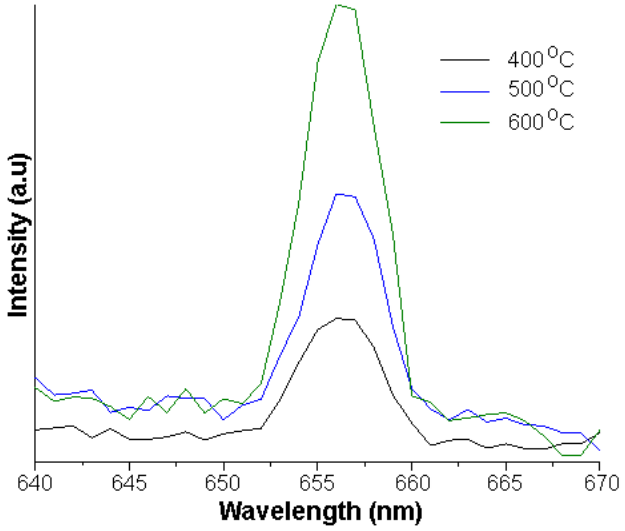

Figure 10. PL spectra of as-prepared samples synthesized by thermal decomposition method at 400, 500, and 600 °C for 2 h.

correlates with reduced recombination of photogenerated charge carriers [86, 87]. However, the PL spectrum of $CuS/Cu_9S_5/Cu_2O/C_3N_4$ composite at 600 °C showed the higher PL emission at 650 – 665 nm, suggesting that the $CuS/Cu_9S_5/Cu_2O/C_3N_4$ composite at 600 °C is more effective separation of the photo-induced charge carrier than other multiphase Cu-based composites due to the formation of quaternary heterojunction $CuS/Cu_9S_5/Cu_2O/C_3N_4$ composites enables trapping and temporary retention of photo-induced charge carrier form the different localized band gap between different phases, thereby enhancing the photocatalytic performance in quaternary heterojunction $CuS/Cu_9S_5/Cu_2O/C_3N_4$ composites [73, 88]. Previous studies have shown that ZnO/CuSe exhibits higher PL intensity than pure ZnO or CuSe, as ZnO/CuSe nanocomposites act as multiple electron traps, reducing photo-generated charge carrier recombination [88]. Among these samples, the $CuS/Cu_9S_5/Cu_2O/C_3N_4$ composite at 600 °C showed the highest MO degradation performance, which can be attributed to its smallest crystallite size, highest visible light harvesting, and efficient electron transfer between the photocatalyst by formation of quaternary composite [89, 90].

The kinetic reactions of MO photocatalytic degradation over heterojunction multiphase Cu-based composites at 400 – 600 °C under visible light irradiation were studied on the Langmuir-Hinshelwood model [91, 92]. The Langmuir-Hinshelwood equation, as a pseudo-first-order kinetics, is usually used to describe the reaction rate by the following equation (3):

$$\ln(C_0/C_t) = k_{app}t \quad (3)$$

where k_{app} is the pseudo-first-order rate constant (min^{-1}) [73, 75, 93]. Fig. 9 (b) shows the linear fitting plots of $\ln(C_t/C_0)$ versus irradiation time (t) for MO degradation across all photocatalysts. The correlation coefficients (R^2) $\geq$ 0.90, confirming that all kinetic reactions of photocatalysis were applicable to the pseudo-first-order Langmuir-Hinshelwood model [90, 94]. The pseudo-first-order rate constant (k) for MO photodegradation over heterojunction multiphase Cu-based composites under visible light irradiation were determined from the linear slopes and calculated as 2.47×10^{-3}, 4.14×10^{-3}, 0.0110, 0.0128, 0.0158, and 9.45×10^{-3} min^{-1} for heterojunction multiphase Cu-based composites at 400, 450, 500, 550, 600 and 650 °C, respectively [90, 94]. Among these, the heterostructure $CuS/Cu_9S_5/Cu_2O/C_3N_4$ at 600 °C was the highest pseudo-first-order rate constant ($k = 0.0158$ min^{-1}), indicating the most efficient photocatalytic degradation. This enhancement is attributed to the improved separation efficiency of photo-generated charge carriers, facilitated by the formation of heterojunction multiphase Cu-based composites.

The effect of pH on the photocatalytic degradation of MO over the $CuS/Cu_9S_5/C_3N_4/Cu_2O$ composite was investigated, as shown in Fig. 11. The initial pH of MO solution over $CuS/Cu_9S_5/C_3N_4/Cu_2O$ composite was 7.30 which adjusted to 5.00 and 6.00 using 1 M HCl and to 8.00 and 9.00 using 1 M NaOH. It was observed that the photocatalytic efficiency of MO over $CuS/Cu_9S_5/C_3N_4/Cu_2O$ composite was decreased in acidic conditions due to the copper sulfide component being unstable in acidic conditions, which decomposed into Cu^{2+} ions and H_2S as products [47, 49]. Conversely, in alkaline conditions, the photocatalytic efficiency of MO over $CuS/Cu_9S_5/C_3N_4/Cu_2O$ composite was decreased to 67.17% at pH 8 and 18.87% at pH 9 due to the OH^- ions were replaced the absorbed MO molecules as anion dye on the surface of $CuS/Cu_9S_5/C_3N_4/Cu_2O$ composite. Therefore, the maximum MO degradation efficiency was achieved at neutral pH (7.30), without additional pH adjustments. This suggests that the $CuS/Cu_9S_5/C_3N_4/Cu_2O$ composite is optimally effective under neutral conditions, making it more practical for real-world applications. Table 2 compares the photocatalytic efficiency and kinetic rate constant of as-prepared $CuS/Cu_9S_5/Cu_2O/C_3N_4$ composite with previously reported Cu-based photocatalysts [95–100]. The results indicate that the as-prepared $CuS/Cu_9S_5/Cu_2O/C_3N_4$ sample exhibits superior photo-

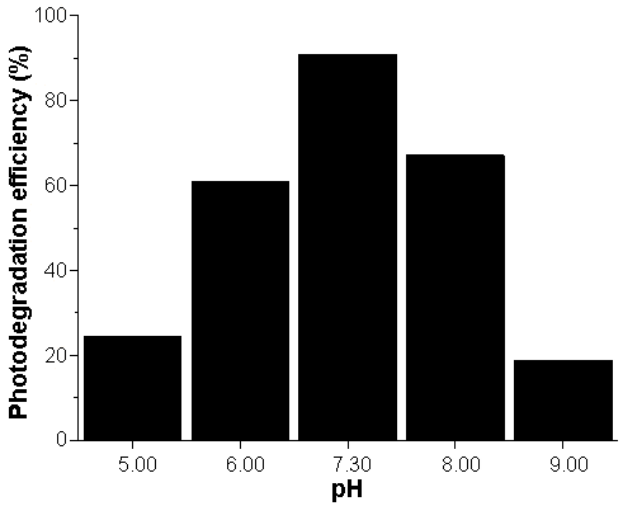

Figure 11. Effect of pH on photedegradation efficiencies of MO over $CuS/Cu_9S_5/Cu_2O/C_3N_4$ composite under visible light irradiation.

Table 2. Photocatalytic comparison of as-prepared $CuS/Cu_9S_5/Cu_2O/C_3N_4$ sample at 600 °C and previous reports.

Photocatalyst	Dye	Light	Photocatalytic degradation (%)	Kinetic rate constant (min^{-1})	Reference
C_3N_4/0.50 wt% CuS	MO	Visible light	53.9% within 60 min	0.0136	95
Cu_2S flakes	MO	Visible light	90% within 300 min	0.0070	96
Cu_9S_5	MO	Solar simulator	88% within 180 min	0.0112	97
	Methylene blue (MB)		~80% within 240 min	0.0090	
Cu_2S	MO		67% within 180 min	0.0067	
	MB		~77% within 240 min	0.0062	
CuO	MO	UV light	~80% within 150 min	0.0099	98
Cu_2O	MO	Visible light	~96% within 240 min	0.0127	99
SnO_2-ZnO-Cu_2S thin film	MO	UV light	26% within 360 min	-	100
	MB		42% within 360 min	-	
$CuS/Cu_9S_5/Cu_2O/C_3N_4$	MO	Visible light	90.06% within 150 min	0.0158	This work

catalytic performance and a higher kinetic rate constant than both single-phase and multiphase Cu-based photocatalysts. This enhancement is attributed to the higher visible light absorption and efficient charge carrier separation due to the formation of a quaternary heterojunction structure [95–100]. According to the Shi et al. reports [101, 102], the multicomponent photocatalyst showed better photocatalytic performance than a single photocatalyst, which creates an internal electric field between the semiconductor materials with different bandgap energies to accelerate the effective photo-carrier separation and great redox ability, enhancing the photocatalytic reaction of S-scheme junction photocatalyst.

The degradation products of MO after photocatalytic reaction over $CuS/Cu_9S_5/Cu_2O/C_3N_4$ at 600 °C were analyzed using direct mass spectroscopy in negative ion mode, as shown in Fig. 12. The mass spectrum of the pure MO solution shows a peak at m/z = 306, corresponding to the 304.07 which is corresponding to the sulfonate anion of methyl orange [103, 104]. However, the intensity of the m/z = 306 peak gradually decreased over the course of the photocatalytic reaction from 30 to 90 min, indicating that the structure of MO was degraded by active species during the photocatalytic reaction [105–107]. After 150 min of irradiation, it found the small aliphatic chain organic molecules with m/z at 290.06, 276.04, 265.14, 248.96, 199.00, 172.99, and 154.97, which indicate that the MO was chromophore cleavage, open ring, which would further mineralize into CO_2, H_2O, and non-toxic inorganic ions as the final products.

The reusable and stability of the $CuS/Cu_9S_5/Cu_2O/C_3N_4$ composite at 600 °C were evaluated by monitoring MO degradation over five cycles under visible light irradiation, as shown in Fig. 13 (a). The photodegradation efficiency of MO in the presence of the $CuS/Cu_9S_5/Cu_2O/C_3N_4$ composite at 600 °C slightly decreased from 90.02% in the first cycle to 85.89% in the fifth cycle, demonstrating high stability and reusability for practical photocatalytic application [73, 89, 108]. To further assess the structural stability of the $CuS/Cu_9S_5/Cu_2O/C_3N_4$ composite at 600 °C after five photocatalytic cycles, its phase and crytallinity of reused $CuS/Cu_9S_5/Cu_2O/C_3N_4$ composite at 600 °C were characterized by XRD, as shown in Fig. 13 (b). The XRD pattern of the reused $CuS/Cu_9S_5/Cu_2O/C_3N_4$ composite at 600 °C exhibited diffraction peaks similar to those of the fresh composite at 600 °C, indicating that its

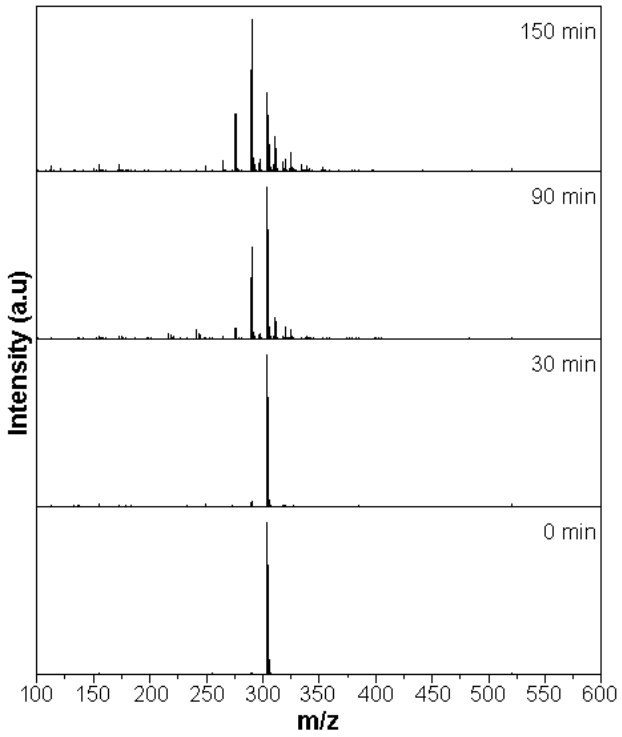

Figure 12. Mass spectra of MO over $CuS/Cu_9S_5/Cu_2O/C_3N_4$ composite at 600 °C for under visible light irradiation at 0, 30, 90 and 150 min.

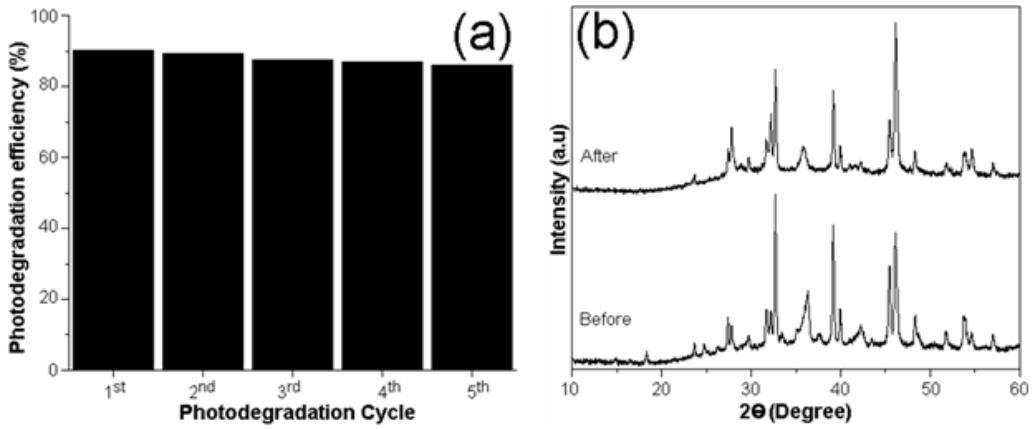

Figure 13. (a) The photostability testing and (b) XRD pattern of reused $CuS/Cu_9S_5/Cu_2O/C_3N_4$ composite for MO degradation under visible light irradiation.

phase composition and crystal structure remain unchanged after five cycles of photocatalytic reaction. The sharp diffraction peaks in the reused sample confirm that the $CuS/Cu_9S_5/Cu_2O/C_3N_4$ composite at 600 °C retains high crystallinity, further supporting its long-term stability in photocatalytic applications. These results indicate that the $CuS/Cu_9S_5/Cu_2O/C_3N_4$ composite at 600 °C exhibits excellent photocatalytic potential under visible light irradiation and is a promising candidate for industrial implementation in both batch and continuous-flow reactor systems [86, 108].

Additionally, the reactive species involved in the photocatalytic degradation of MO over the $CuS/Cu_9S_5/C_3N_4/Cu_2O$ composite at 600 °C under visible light irradiation were identified through scavenger testing. Specifically, sodium oxalate ($Na_2C_2O_4$) was used as a hole (h^+) scavenger, isopropyl alcohol (IPA) for hydroxyl radicals ($^{\bullet}OH$) trapping, and benzoquinone (BQ) for superoxide anions ($^{\bullet}O_2^-$) trapping [109, 110]. Fig. 14 presents the photodegradation efficiencies of MO degradation over $CuS/Cu_9S_5/Cu_2O/C_3N_4$ composite under visible light irradiation, both with and without the addition of $Na_2C_2O_4$, IPA, and BQ. Obviously, the photodegradation efficiency of the $CuS/Cu_9S_5/Cu_2O/C_3N_4$ composite was significantly restrained to 10.55% in the presence of BQ, indicating that superoxide anions ($^{\bullet}O_2^-$) play a crucial role in MO degradation. In contrast, the photodegradation efficiency decreased moderately to 50.12% upon the addition of $Na_2C_2O_4$, suggesting that holes (h^+) also contribute, but to a lesser extent. However, the addition of IPA had a negligible effect, as the photodegradation efficiency remained at 89.46%, confirming that hydroxyl radicals ($^{\bullet}OH$) are not significantly involved in the degradation process. These results indicate that $^{\bullet}O_2^-$ serve as the primary active species, while holes (h^+) act as secondary contributors in the photocatalytic degradation of MO by the $CuS/Cu_9S_5/Cu_2O/C_3N_4$ composite under visible light irradiation [108, 111].

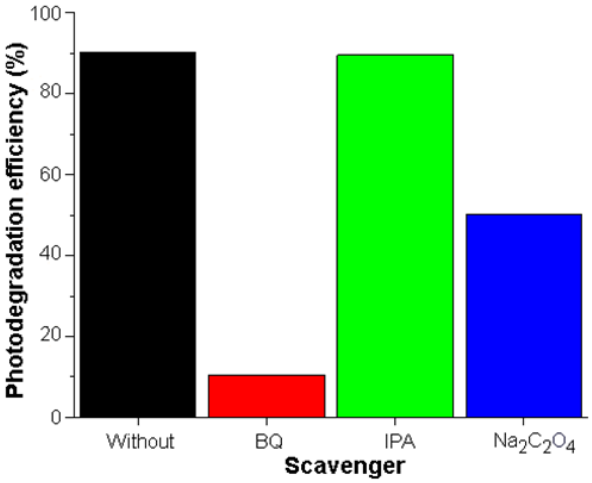

Figure 14. Scavenger test for MO degradation over $CuS/Cu_9S_5/Cu_2O/C_3N_4$ composite under visible light irradiation.

Fig. 15 presents a schematic diagram illustrating the proposed mechanism of visible-light-driven $CuS/Cu_9S_5/Cu_2O/C_3N_4$ photocatalyst. Under light irradiation, photo-generated electrons and holes are created in conduction band (CB) and valence band (VB) of Cu_2O ($E_{VB} = 1.9$ eV and $E_{CB} = -0.3$ eV [112, 113]), CuS ($E_{VB} = 2.0$ eV and $E_{CB} = 0.2$ eV [114]) and Cu_9S_5 ($E_{VB} = 2.6$ eV and $E_{CB} = 1.2$ eV [115]). The photo-generated electrons in the CB of Cu_2O migrate to the CB of CuS and Cu_9S_5, as the CB potential of Cu_2O is higher than that of CuS and Cu_9S_5. These electrons transfer effectively suppresses photo-induced charge carrier recombination within the composite [110, 116]. Subsequently, the photo-generated electrons in the CB of Cu_9S_5 are transferred to C_3N_4, which acts as an electron acceptor, further improving photo-induced charge carrier separation and enhancing the photocatalytic reaction. After that, the photo-generated electrons in C_3N_4 were reacted with the absorbed O_2 molecules on the surface of the composite to generate $^{\bullet}O_2^-$ active species for MO degradation [67, 81]. Simultaneously, the photo-generated holes accumulate in the VB of Cu_2O, as its of VB potential is lower than those of of CuS and Cu_9S_5. These holes react with OH^-/H_2O, generating hydroxyl radicals ($^{\bullet}OH$), which further oxidize MO, ultimately degrading it into CO_2 and H_2O as a final product [90, 117, 118]. Thus, the formation of a quaternary heterojunction $CuS/Cu_9S_5/Cu_2O/C_3N_4$ composite signifi-

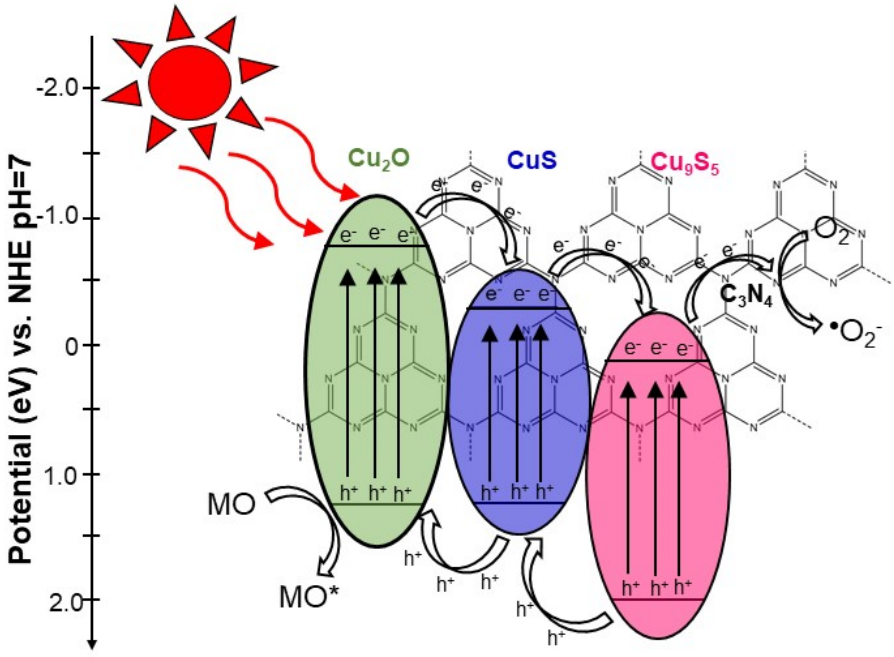

Figure 15. Schematic illustration of photocatalytic reaction of $CuS/Cu_9S_5/Cu_2O/C_3N_4$ composite.

cantly enhances photo-induced charge carrier separation and prolongs the lifetime of photo-induced electrons at the heterojunction interface, thereby improving photocatalytic efficiency.

4. Conclusion

In summary, the novel quaternary heterojunction $CuS/Cu_9S_5/Cu_2O/C_3N_4$ composite was successfully prepared by thermal decomposition of Cu-thiourea (pentakis(thiourea)dicopper(I)sulfate) compound in N_2 atmosphere. The analytic results confirmed the formation of heterojunction $CuS/Cu_9S_5/Cu_2O/C_3N_4$ composite, which revealed the mixed sheets and spherical particles in shape. The quaternary heterojunction $CuS/Cu_9S_5/Cu_2O/C_3N_4$ composite at 600 °C for 2 h demonstrated the highest MO degradation under visible light irradiation. Finally, he $CuS/Cu_9S_5/Cu_2O/C_3N_4$ quaternary composite exhibited excellent photocatalytic performance, with high degradation efficiency, stability, and reusability under visible light irradiation.

Acknowledgements
Prakasit Intaphong would like to acknowledge the Science Achievement Scholarship of Thailand (SAST). Pasu Inphak would like to acknowledge Royal Golden Jubilee PhD (RGJ) scholarship. This research work was partially supported by Chiang Mai University.

Authors contributions
Prakasit Intaphong: Conceptualization, Writing–original draft, Methodology, Validation, Data curation, Investigation, Formal analysis. Pasu Inphak: Formal analysis. Sujitra Tandorn: Formal analysis. Pongpen Kaewdee: Formal analysis. Komsanti Chokethawai: Conceptualization, Supervision. Chamnan Randorn: Writing–original draft, Validation, Supervision, Validation, Funding acquisition, Conceptualization.

Availability of data and materials
Data is available on request from the corresponding author, upon reasonable request.

Conflict of interests
The authors declare that they have no known competing financial interests or personal relationships that could have appeared to influence the work reported in this paper.

References

[1] X. Li, R. Li, and X. Feng. *Russ. J. Inorg. Chem.*, **68(10)**(2023): 1386–1398, .
DOI: https://doi.org/10.1134/S0036023623601307.

[2] A. Gharebaghai, A. H. J. Magham, and L. Hokmabadi. *Russ. J. Phys. Chem. A.*, **97**(2023):3212–3218.
DOI: https://doi.org/10.1134/s0036024424010072.

[3] L. Lianmawi and N. M. Singh. *Russ. J. Phys. Chem. B.*, **18**(2023): 325–342.
DOI: https://doi.org/10.1134/S1990793124010329.

[4] S. Amin, R. P. Rastogi, and M. G. Chaube K. Jain. *Front. Microbiol.*, **11**(2020):1–12.

[5] R. Kishor, D. Purchase, G. D. Saratale, L. F. R. Ferreira, C. M. Hussain, S. I. Mulla, and R. N. Bharagava. *J. Water Process Eng.*, **43**(2021):102300.
DOI: https://doi.org/10.1016/j.jwpe.2021.102300.

[6] I. Ayadi, Y. Souissi, I. Jlassi, F. Peixoto, and W. Mnif. *J. Dev. Drugs.*, **5**(2016):1000151.
DOI: https://doi.org/10.4172/2329-6631.1000151.

[7] A. Maruthanayagam, P. Mani, K. Kaliappan, and S. Chinnappan. *Water Air Soil Pollut.*, **132**(2020):231.
DOI: https://doi.org/10.1007/s11270-020-04585-z.

[8] Md. M. Haque, Md. A. Haque, Md K. Mosharaf, and P. K. Marcus. *Saudi J. Biol. Sci.*, **28**(2021):793–804.
DOI: https://doi.org/10.1016/j.sjbs. 2020.11.012.

[9] J. S. Sravan, L. Matsakas, and O. Sarkar. *Bioengineering*, **11**(2024): 281.
DOI: https://doi.org/10.3390/bioengineering11030281.

[10] A. Khalidi idrissi, A. Madinzi, A. Anouzla, A. Pala, L. Mouhir, Y. Kadmi, and S. Souabi. *Int. J. Environ. Sci. Technol.*, **20**(2023): 11719–11740.
DOI: https://doi.org/10.1007/s13762-023-04867-z.

[11] S. Kanmani and A. G. B. Dileepan. *J. Environ. Manage.*, **345**(2023): 118794.
DOI: https://doi.org/10.1016/j.jenvman.2023.118794.

[12] J. Iyyappan, B. Gaddala, R. Gnanasekaran, M. Gopinath, D. Yuvaraj, and V. Kumar. *Case Stud. Chem. Environ. Eng.*, **9**(2024): 100599.
DOI: https://doi.org/10.1016/j.cscee.2023.00599.

[13] M. Pavel, C. Anastasescu, R. N. State, A. Vasile, F. Papa, and I. Balint. *Catalysts*, **13**(2023):380.
DOI: https://doi.org/10.3390/catal13020380.

[14] C. Shen, X. Li, B. Xue, D. Feng, Y. Liu, F. Yang, M. Zhang, and S. Li. *Appl. Surf. Sci.*, **679**(2025):161303.
DOI: https://doi.org/10.1016/j.apsusc.2024.161303.

[15] J. Zhang, G. Yu, C. Yang, and S. Li. *Curr. Opin. Chem. Eng.*, **45**(2024):101040, .
DOI: https://doi.org/10.1016/j.coche.2024.101040.

[16] S. Li, K. Dong, M. Cai, X. Li, and X. Chen. *eScience*, **4(2)**(2024): 100208, .
DOI: https://doi.org/10.1016/j.esci.2023.100208.

[17] W. Shi, S. Yang, H. Sun, J. Wang, X. Lin, F. Guo, and J. Shi. *J. Mater. Sci.*, **56**(2021):2226–2240, .
DOI: https://doi.org/10.1007/s10853-020-05436-2.

[18] F. Guo, X. Huang, Z. Chen, L. Cao, X. Cheng, L. Chen, and W. Shi. *Sep. Purif. Technol.*, **265**(2021):118477.
DOI: https://doi.org/10.1016/j.seppur.2021. 118477.

[19] N. S. Choudhari, R. U. Mene, P. P. Bardapurkar, and S. N. Dalvi. *Appl. Phys. A.*, **130**(2024):874.
DOI: https://doi.org/10.1007/s00339-024-08043-z.

[20] M. A. Ansari, M. Shariq, S. S. Ansari, and A. Husain. *Environ. Sci. Pollut. Res.*, (2024).
DOI: https://doi.org/10.1007/s11356-024-35538-2.

[21] M. Jeevarathinam and I. V. Asharani. *Sci. Rep.*, **14**(2024):9718.
DOI: https://doi.org/10.1038/s41598-024-60008-7.

[22] V. Gautam, A. Kumar, S. Nagpal, and V. K. Jain. *J. Alloys Compd.*, **919**(2022):165840.
DOI: https://doi.org/10.1016/j.jallcom.2022.165840.

[23] M. M. Sayed, A. M. Aboraia, Y. A. Kasem, N. N. Elewa, Y. A. M. Ismail, and K. I. Aly. *Sci. Rep.*, **14**(2024):12768.
DOI: https://doi.org/10.1038/s41598-024-61983-7.

[24] I. Abdelfattah and A. M. El-Shamy. *Sci. Rep.*, **14**(2024):27175.
DOI: https://doi.org/10.1038/s41598-024-77752-5.

[25] J. Wang, H. Wang, C. Liu, Z. Jiang, X. Liu, Z. Kang, Z. Hao, Q. Feng, and L. Xu. *J. Sol-Gel Sci. Technol.*, (2024), .
DOI: https://doi.org/10.1007/s10971-024-06436-3.

[26] T. Haj, K. Sadraoui, K. Mejdoubi, A. E. Yacoubi, B. C. E. Idrissi, and B. Sallek. *Res. Chem. Intermediat*, (2024).
DOI: https://doi.org/10.1007/s11164-024-05443-x.

[27] A. K. Sibhatu, G. K. Weldegebrieal, S. Sagadevan, N. N. Tran, and V. Hessel. *Chemosphere*, **300**(2022):134623.
DOI: https://doi.org/10.1016/j. chemosphere.2022.134623.

[28] S. Aroob, S. A. C. Carabineiro, M. B. Taj, I. Bibi, A. Raheel, T. Javed, R. Yahya, W. Alelwani, F. Verpoort, K. Kamwilaisak, S. Al-Farraj, and M. Sillanpää. *Catalysts*, **13**(2023):502.
DOI: https://doi.org/10.3390/catal13030502.

[29] N. Bhat, S. J. Ukkund, M. Ashraf, K. Acharya, N. J. Ramegouda, P. Puthiyillam, M. A. Hasan, S. Islam, V. B. Koradoor, A. D. Praveen, and M. A. Khan. *ACS Omega*, **8**(2023):32512–32519.
DOI: https://doi.org/10.1021/acsomega.3c02598.

[30] S. Li, J. H. Lee, S. M. Hwang, and Y. J. Kim. *Nano Converg*, **10**(2023):4, .
DOI: https://doi.org/10.1186/s40580-022-00353-3.

[31] G. Wisz, P. Sawicka-Chudy, A. Wal, M. Sibi´nski, P. Potera, R. Yavorskyi, L. Nykyruy, D. Płoch, M. Bester, M. Cholewa, and O. M. Chernikova. *Appl. Sci.*, **13**(2023):3613.
DOI: https://doi.org/10.3390/app13063613.

[32] L. Isac, C. Cazan, L. Andronic, and A. Enesca. *Catalysts*, **12**(2022): 1135.
DOI: https://doi.org/10.3390/catal12101135.

[33] R. A. El Gendy, H. M. El Bery, M. Farrag, and D. M. Fouad. *Sci. Rep.*, **13**(2023):7994.
DOI: https://doi.org/10.1038/s41598-023-34743-2.

[34] M. Yusuf, S. A. Hira, and K. H. Park. *ACS Appl. Mater. Interfaces*, **14**(2022):15529–15540.
DOI: https://doi.org/10.1021/acsami.2c00279.

[35] C. Wu, Y. Sun, Z. Cui, F. Song, and J. Wang. *J. Phys. Chem. Solids*, **140**(2020):109355, .
DOI: https://doi.org/10.1016/j.jpcs.2020.109355.

[36] M. Abdullah, P. John, M. N. Ashiq, S. Manzoor, M. I. Ghori, M. U. Nisa, A. G. Abid, K. Y. Butt, and S. Ahmed. *Nanotechnol. Environ. Eng.*, **8**(2023):63–73.
DOI: https://doi.org/10.1007/s41204-022-00266-w.

[37] Y. Gu, T. Li, B. Guo, Y. Jiang, W. Wen, J. Wu, and L. Zhao. *Cryst. Eng. Comm.*, **22**(2020):7082.
DOI: https://doi.org/10.1039/D0CE01059F.

[38] G. Kalimuldina, A. Nurpeissova, A. Adylkhanova, D. Adair, I. Taniguchi, and Z. Bakenov. *ACS Appl. Energy Mater.*, **3**(2020): 11480–11499.
DOI: https://doi.org/10.1021/acsaem.0c01686.

[39] L. Chaperman, S. Chaguetmi, B. Deng, S. G. Derrouich, S. Nowak, F. Mammeri, and S. Ammar. *Nanomaterials*, **14**(2024):1581.
DOI: https://doi.org/10.3390/ nano14191581.

[40] G. Y. Shaikh, D. S. Nilegave, S. S. Girawale, K. B. Kore, S. R. Newaskar, S. A. Sahu, and A. M. Funde. *ACS Omega*, **7**(2022): 30233–30240.
DOI: https://doi.org/10.1021/acsomega.2c03352.

[41] S. Kumar Bhawna, A. Gupta, R. Kumar, A. Bharti, A. Kumar, and V. Kumar. *J. Phys. Chem. C.*, **127**(2023):7095–7106.
DOI: https://doi.org/10.1021/acs.jpcc.2c08094.

[42] C. You, C. Wang, M. Cai, Y. Liu, B. Zhu, and S. Li. *Acta Phys.-Chim. Sin.*, **40(11)**(2024):2407014.
DOI: https://doi.org/10.3866/PKU.WHXB202407014.

[43] C. Wang, Rong K, Y. Liu, F. Yang, and S. Li. *Sci. China Mater.*, **67(2)**(2024):562–572, .
DOI: https://doi.org/10.1007/s40843-023-2764-8.

[44] L. Han, W. Zhan, X. Liang, W. Zhang, R. Huang, R. Chen, and H. Ni. *Ceram. Int.*, **48**(2022):22018–22030.
DOI: https://doi.org/10.1016/j.ceramint.2022.04.192.

[45] C. Wang, W. Xu, C. Xu, Q. Zhang, Z. Zhang, X. Wang, Z. Fan, and X. Xiong. *J. Mater. Sci.*, **57**(2022):15314–15330, .
DOI: https://doi.org/10.1007/s10853-022-07593-y.

[46] S. Mosleh, M. R. Rahimi, M. Ghaedi, K. Dashtian, and S. Hajati. *Ultrason. Sonochem*, **40**(2018):601–610.
DOI: https://doi.org/10.1016/j.ultsonch.2017.08.007.

[47] J. Li, Y. He, and Y. Zhao. *Russ. J. Phys. Chem., A.*, **98**(2024):2380–2389, .
DOI: https://doi.org/10.1134/S0036024424701553.

[48] W. Iqbal, B. Yang, X. Zhao, M. Rauf, M. Waqas, Y. Gong, J. Zhang, and Y. Mao. *Catal. Sci. Technol.*, **8**(2018):4576–4599.
DOI: https://doi.org/10.1039/C8CY01061G.

[49] H. M. Mukhair, A. H. Abdullah, Z. Zainal, and H. N. Lim. *Polymers*, **13**(2021):1746.
DOI: https://doi.org/10.3390/polym1311174.

[50] J. F. Catalá, R. Greco, M. N. García, W. Cao, Á. B. Murcia, and D. C. Amorós. *Catalysts*, **12**(2022):1137.
DOI: https://doi.org/10.3390/catal12101137.

[51] M. Cai, Y. Liu, K. Dong, X. Chen, and S. Li. *Chinese J. Catal.*, **52**(2023):239–251.
DOI: https://doi.org/10.1016/S1872-2067(23)64496-1.

[52] W. Shi, K. Shu, H. Sun, H. Ren, M. Li, F. Chen, and F. Guo. *Sep. Purif. Technol.*, **246**(2020):116930, .
DOI: https://doi.org/10.1016/j.seppur.2020.116930.

[53] W. Shi, M. Li, X. Huang, H. Ren, C. Yan, and F. Guo. *Chem. Eng. J.*, **382**(2020):122960, .
DOI: https://doi.org/10.1016/j.cej.2019.122960.

[54] Md. A. Hanif, J. Akter, Y. S. Kim, H. G. Kim, J. R. Hahn, and L. K. Kwac. *Catalysts*, **12**(2022):151.
DOI: https://doi.org/10.3390/catal12020151.

[55] E. V. Siddhardhan, A. Steephen, and T. Arumanayagam. *J. Mater. Sci.: Mater. Electron.*, **34**(2023):1225, .
DOI: https://doi.org/10.1007/s10854-023-10649-7.

[56] Y. Si, X. Zhang, T. Liang, X. Xu, L. Qiu, P. Li, and S. Duo. *Mater. Res. Express.*, **7**(2020):015524.
DOI: https://doi.org/10.1088/2053-1591/ab6893.

[57] M. H. Suhag, A. Khatun, I. Tateishi, M. Furukawa, H. Katsumata, and S. Kaneco. *ACS Omega*, **8**(2023):11824–11836.
DOI: https://doi.org/10.1021/acsomega.2c06678.

[58] W. Shi, C. Liu, M. Li, X. Lin, F. Guo, and J. Shi. *J. Hazard. Mater.*, **389**(2020):121907, .
DOI: https://doi.org/10.1016/j.jhazmat.2019.121907.

[59] R. Zhang, Y. Wu, J. Pei, Z. H. Ge, B. P. Zhang, Q. Sunc, and G. Nie. *Cryst. Eng. Comm.*, **21**(2019):5797–5803, .
DOI: https://doi.org/10.1039/C9CE00936A.

[60] P. Kumar, M. Gusain, and R. Nagarajan. *Inorg. Chem.*, **50**(2011):3065–3070.
DOI: https://doi.org/10.1021/ic102593h.

[61] Y. Hong, E. Liu, J. Shi, X. Lin, L. Sheng, M. Zhang, L. Wang, and J. Chen. *Int. J. Hydrogen Energ.*, **44**(2019):7194–7204.
DOI: https://doi.org/10.1016/ j.ijhydene.2019.01.274.

[62] M. P. Ravele, O. A. Oyewo, and D. C. Onwudiwe. *Catalysts*, **11**(2021):899.
DOI: https://doi.org/10.3390/catal11080899.

[63] C. M. Simonescu, V. S. Teodorescu, O. Carp, L. Patronand, and C. Capatina. *J. Therm. Anal. Calorim.*, **88**(2007):71–76.
DOI: https://doi.org/10.1007/s10973-006-8079-z.

[64] E. V. Siddhardhan, A. Steephen, and T. Arumanayagam. *J. Mater. Sci.: Mater. Electron.*, **34**(2023):1225, .
DOI: https://doi.org/10.1007/s10854-023-10649-7.

[65] X. Liu, X. Xu, H. Gan, M. Yu, and Y. Huang. *Catalysts*, **13**(2023):848, .
DOI: https://doi.org/10.3390/catal13050848.

[66] Y. Ma, J. Zhang, Y. Wang, Q. Chen, Z. Feng, and T. Sun. *J. Adv. Res.*, **16**(2019):135–143, .
DOI: https://doi.org/10.1016/j.jare.2018.10.003.

[67] A. A. Dubale, A. G. Tamirat, H. M. Chen, T. A. Berhe, C. J. Pan, W. N. Su, and B. J. Hwang. *J. Mater. Chem. A.*, **4**(2016):2205–2216.
DOI: https://doi.org/10.1039/c5ta09464j.

[68] N. Karikalan, R. Karthik, S. M. Chen, C. Karuppiah, and A. Elangovan. *Sci. Rep.*, **7**(2017):2494.
DOI: https://doi.org/10.1038/s41598-017-02479-5.

[69] G. Panzeri, M. Cristina, M. S. Jagadeesh, G. Bussetti, and L. Magagnin. *Sci. Rep.*, **10**(2020):18730.
DOI: https://doi.org/10.1038/s41598-020-75700-7.

[70] S. Gahlot, B. Purohit, E. Jeanneau, and S. Mishra. *Chem. Eur. J.*, **27**(2021):10779.
DOI: https://doi.org/10.1002/chem.202102278.

[71] C. Liang, X. Li, J. Han, N. Ye, H. Liu, H. Feng, L. Huang, Y.Liu, and X. Peng. *J. Alloys Compd.*, **883**(2021):160816.
DOI: https://doi.org/10.1016/j.jallcom.2021.160816.

[72] A. W. Kahsay, K. B. Ibrahim, M. C. Tsai, M. K. Birhanu, S. A. Chala, W. N. Su, and B. J. Hwang. *Catal. Lett.*, **149**(2019):860–869.
DOI: https://doi.org/10.1007/s10562-019-02657-2.

[73] N. Akter, T. Ahmed, I. Haque, Md K. Hossain, G. Ray, Md M. Hossain, Md S. Islam, Md A. A. shaikh, and U. S. Akhtar. *Heliyon*, **10**(2024):e30802.
DOI: https://doi.org/10.1016/j.heliyon.2024.e30802.

[74] S. Li, R. Yan, M. Cai, W. Jiang, M. Zhang, and X. Li. *J. Mater. Sci. Technol.*, **164**(2023):59–67, .
DOI: https://doi.org/10.1016/j.jmst.2023.05.009.

[75] X. Tao, Y. Wu, and H. Sha. *Water Air Soil Pollut.*, **229**(2018):322.
DOI: https://doi.org/10.1007/s11270-018-3977-9.

[76] S. Liu, H. Hou, X. Liu, J. Duan, Y. Yao, and Q. Liao. *Ionics*, **23**(2017):1075–1082, .
DOI: https://doi.org/10.1007/s11581-016-1933-5.

[77] Ö. Tunaa, E. B. Simsek, I. Dashan, and G. Temel. *J. Photoch. Photobio. A.*, **396**(2020):112519.
DOI: https://doi.org/10.1016/j.jphotochem.2020.112519.

[78] X. Zhu, F. Yang, J. Liu, G. Zhou, D. Chen, Z. Liu, and J. Fang. *Catalysts*, **12**(2022):1583.
DOI: https://doi.org/10.3390/catal12121583.

[79] L. Tan, J. Xu, X. Zhang, Z. Hang, Y. Jia, and S. Wang. *Appl. Surf. Sci.*, **356**(2015):447–453.
DOI: https://doi.org/10.1016/j.apsusc.2015.08.078.

[80] Y. Xu, F. Ge, Z. Chen, S. Huang, W. Wei, M. Xie, H. Xu, and H. Li. *Appl. Surf. Sci.*, **469**(2019):739–746, .
DOI: https://doi.org/10.1016/j.apsusc.2018.11.062.

[81] D. C. Onwudiwe, O. C. Olatunde, V. M. Nkwe, Y. B. Smida, and H. Ferjani. *Inorg. Chem. Commun.*, **155**(2023):111075.
DOI: https://doi.org/10.1016/j.inoche.2023.111075.

[82] T. Morikawa, R. Asahi, T. Ohwaki, K. Aoki, and Y. Taga. *Jpn. J. Appl. Phys.*, **40**(2001):561–563.
DOI: https://doi.org/10.1143/JJAP.40.L561.

[83] Z. Zhong, R. Xu, H. He, Q. Zhuang, and L. Huang. *Desalin. Water Treat.*, **137**(2019):234–242.
DOI: https://doi.org/10.5004/dwt.2019.23160.

[84] B. Rhimi, C. Wang, and D. W. Bahneman. *J. Phys. Energy*, **2**(2020): 042003.
DOI: https://doi.org/10.1088/2515-7655/abb782.

[85] Q. Wang, Y. Li, F. Huang, S. Song, G. Ai, X. Xin, B. Zhao, Y. Zheng, and Z. Zhang. *Molecules*, **28**(2023):432, .
DOI: https://doi.org/10.3390/molecules28010432.

[86] X. Zhang, F. Qin, Y. Zhong, T. Xiao, Q. Yu, X. Zhu, W. Feng, and Z. Qi. *Molecules*, **29**(2024):4911, .
DOI: https://doi.org/10.3390/molecules29204911.

[87] A. Priya, R. A. Senthil, A. Selvi, P. Arunachalam, C. K. S. Kumar, J. Madhavan, R. Boddula, R. Pothu, and A. M. Al-Mayouf. *Mater. Sci. Energy Technol.*, **3**(2020):43–50.
DOI: https://doi.org/10.1016/j.mset.2019.09.013.

[88] K. Mubeen, K. Safeen, A. Irshad, A. Safeen, T. Ghani, W. H. Shah, R. Khan, K. S. Ahmad, R. Casin, M. A. Rashwan, H. O. Elansary, and A. Shah. *Sci. Rep.*, **13**(2023):19580.
DOI: https://doi.org/10.1038/s41598-023-46780-y.

[89] G. Du, Y. Ding, C. Li, L. Zhang, J. Li, M. Li, W. Zhu, and C. He. *Materials*, **17**(2024):4306.
DOI: https://doi.org/10.3390/ma17174306.

[90] A. Sewnet, E. Alemayehu, M. Abebe, D. Mani, S. Thomas, and B. Lennartz. *Materials*, **16**(2023):5497.
DOI: https://doi.org/10.3390/ma16155497.

[91] M. Hassanpour, H. S. Hojaghan, and M. S. Niasari. *J. Mol. Liq.*, **229**(2017):293–299.
DOI: https://doi.org/10.1016/j.molliq.2016.12.090.

[92] P. Patiphatpanya, P. Intaphong, A. Phuruangrat, B. Kuntalue, P. Dumrongrojthanath, T. Thongtem, and S. Thongtem. *Dig. J. Nanomater. Bios.*, **15**(2020):115–121.
DOI: https://doi.org/10.15251/djnb.2020.151.115.

[93] S. Sharafzadeh, J. Zolgharnein, A. N. Ejhieh, and S. D. Farahani. *Int. J. Hydrogen Energy*, **106**(2025):1429–1442.
DOI: https://doi.org/10.1016/j.ijhydene.2025.02.031.

[94] S. Singh, A. K. Atri, I. Qadir, S. Sharma, U. Manhas, and D. Singh. *ACS Omega*, **8**(2023):6302–6317.
DOI: https://doi.org/10.1021/acsomega.2c06249.

[95] Z. Xu, B. Xu, K. Qian, Z. Li, F. Ding, M. Fan, Y. Sun, and Y. Gao. *RSC Adv.*, **9**(2019):25638–25646, .
DOI: https://doi.org/10.1039/C9RA03532J.

[96] M. Telkhozhayeva, R. Konar, R. Lavi, E. Teblum, B. Malik, S. Ruthstein, E. Moretti, and G. D. Nessim. *ACS Sustain. Chem. Eng.*, **9(48)**(2021):16103–16114.
DOI: https://doi.org/10.1021/acssuschemeng.1c04545.

[97] R. K. Sithole, L. F. E. Machogo, M. J. Moloto, S. S. Gqoba, K. P. Mubiayi, J. V. Wyk, and N. Moloto. *J. Photochem. Photobiol. A Chem.*, **397**(2020):112577.
DOI: https://doi.org/10.1016/j.jphotochem.2020.112577.

[98] A. Rajbhandari and G. Neupane. *Sci. World*, **17(17)**(2024):106–113.
DOI: https://doi.org/10.3126/sw.v17i17.66443.

[99] P. K. N. Ho. *Fine Chem. Eng.*, **5**(2024):135–142.
DOI: https://doi.org/10.37256/fce.5120244244.

[100] A. Enesca, L. Isac, and A. Duta. *Thin Solid Films*, **542**(2013): 31–37.
DOI: https://doi.org/10.1016/j.tsf.2013.06.008.

[101] S. Li, K. Rong, X. Wang, C. Shen, F. Yang, and Q. Zhang. *Acta Phys.-Chim. Sin.*, **40**(2024):2403005, .
DOI: https://doi.org/10.3866/PKU.WHXB202403005.

[102] S. Li, C. You, K. Rong, C. Zhuang, X. Chen, and B. Zhang. *Adv. Powder Mater.*, **3**(2024):100183, .
DOI: https://doi.org/10.1016/j.apmate.2024.100183.

[103] D. K. Sarfo, A. Kaur, D. L. Marshall, and A. P. O'Mullane. *Chemosphere*, **316**(2023):137821.
DOI: https://doi.org/10.1016/j.chemosphere.2023.137821.

[104] S. Ghattavi and A. N. Ejhieh. *Int. J. Hydorg. Energy*, **45**(2020): 24636–24656, .
DOI: https://doi.org/10.1016/j.ijhydene.2020.06.207.

[105] T. Chen, Y. Zheng, J. M. Lin, and G. Chen. *J. Am. Soc. Mass Spectrom*, **19(7)**(2011):997–1003.
DOI: https://doi.org/10.1016/j.jasms.2008.03.008.

[106] D. G. Fukina, A. V. Koryagin, D. N. Titaev, E. V. Suleimanov, N. I. Kirillova, A. V. Boryakov, and A. V. Mitin. *Eur. J. Inorg. Chem.*, **28**(2022):e202200371.
DOI: https://doi.org/10.1002/ejic.202200371.

[107] N. N. Bahrudin, M. A. Nawi, and W. I. Nawawi. *Res. Chem. Intermed.*, **45**(2019):2771–2795.
DOI: https://doi.org/10.1007/s11164-019-03762-y.

[108] N. Omrani and A. N. Ejhieh. *J. Water Process Eng.*, **33**(2020): 101094.
DOI: https://doi.org/10.1016/j.jwpe.2019.101094.

[109] X. Zheng, J. Yuan, J. Shen, J. Liang, J. Che, B. Tang, G. He, and H. Chen. *J. Mater. Sci.: Mater. Electron.*, **30**(2019):5986–5994.
DOI: https://doi.org/10.1007/s10854-019-00898-w.

[110] K. I. John, T. B. Issa, G. Ho, A. N. Nikoloski, and D. Li. *Water*, **16**(2024):2563.
DOI: https://doi.org/10.3390/w16182563.

[111] S. Ghattavi and A. N. Ejhieh. *Compos. B Eng.*, **183**(2020):107712, .
DOI: https://doi.org/10.1016/j.compositesb.2019.107712.

[112] C. Hou, J. Xie, H. Yang, S. Chen, and H. Liu. *RSC Adv.*, **9**(2019): 37911–37918.
DOI: https://doi.org/10.1039/c9ra07999h.

[113] Q. Tang, W. Wu, B. Zhang, J. Luo, H. Zhang, X. Guo, J. Jia, and J. Cao. *J. Inorg. Organomet. Polym. Mater.*, **29**(2019):340–345.
DOI: https://doi.org/10.1007/s10904-018-1004-7.

[114] Z. Ma, W. Guo, K. Zhang, N. Wang, Z. Li, and J. Li. *Molecules*, **28**(2023):3084, .
DOI: https://doi.org/10.3390/molecules28073084.

[115] Y. Wang, S. Shen, M. Liu, G. He, and X. Li. *J. Colloid Interf. Sci.*, **655**(2024):187–198, .
DOI: https://doi.org/10.1016/j.jcis.2023.10.164.

[116] D. Jiang, J. Xue, L. Wu, W. Zhou, Y. Zhang, and X. Li. *Appl. Catal. B: Environ.*, **211**(2017):199–204.
DOI: https://doi.org/10.1016/j.apcatb.2017.04.034.

[117] Z. Wu, X. Chen, X. Liu, X. Yang, and Y. Yang. *Nanoscale Res. Lett.*, **14**(2019):147, .
DOI: https://doi.org/10.1186/s11671-019-2974-2.

[118] S. A. Mirsalari and A. N. Ejhieh. *Sep. Purif. Technol.*, **250**(2020): 117235.
DOI: https://doi.org/10.1016/j.seppur.2020.117235.